Robust diffraction-limited near-infrared-to-near-ultraviolet wide-field imaging from stratospheric balloon-borne platforms—Super-pressure Balloon-borne Imaging Telescope performance

L. Javier Romualdez [ID], Steven J. Benton [ID], Anthony M. Brown, Paul Clark, Christopher J. Damaren, Tim Eifler [ID], Aurelien A. Fraisse, Mathew N. Galloway, Ajay Gill, John W. Hartley, Bradley Holder, Eric M. Huff, Mathilde Jauzac [ID], William C. Jones [ID], David Lagattuta [ID], Jason S.-Y. Leung, Lun Li [ID], Thuy Vy T. Luu, Richard J. Massey [ID], Jacqueline McCleary, James Mullaney, Johanna M. Nagy [ID], C. Barth Netterfield, Susan Redmond, Jason D. Rhodes, Jürgen Schmoll, Mohamed M. Shaaban, Ellen Sirks, and Sut-Ieng Tam

View Online **Export Citation** **CrossMark**

ARTICLES YOU MAY BE INTERESTED IN

Influence of extraction grid on ion beam characteristics
Review of Scientific Instruments **91**, 033304 (2020); https://doi.org/10.1063/1.5128599

Measurement of quadrupolar asymmetry in prototype rod-type radio frequency quadrupole linac for protons
Review of Scientific Instruments **91**, 033306 (2020); https://doi.org/10.1063/1.5140630

A multi-stop time-of-flight spectrometer for the measurement of positron annihilation-induced electrons in coincidence with the Doppler-shifted annihilation gamma photon
Review of Scientific Instruments **91**, 033903 (2020); https://doi.org/10.1063/1.5140789

Robust diffraction-limited near-infrared-to-near-ultraviolet wide-field imaging from stratospheric balloon-borne platforms—Super-pressure Balloon-borne Imaging Telescope performance

L. Javier Romualdez,[1,a] Steven J. Benton,[1] Anthony M. Brown,[2,3] Paul Clark,[2] Christopher J. Damaren,[4] Tim Eifler,[5] Aurelien A. Fraisse,[1] Mathew N. Galloway,[6] Ajay Gill,[7,8] John W. Hartley,[9] Bradley Holder,[4,8] Eric M. Huff,[10] Mathilde Jauzac,[3,11] William C. Jones,[1] David Lagattuta,[3] Jason S.-Y. Leung,[7,8] Lun Li,[1] Thuy Vy T. Luu,[1] Richard J. Massey,[2,3,11] Jacqueline McCleary,[10] James Mullaney,[12] Johanna M. Nagy,[8] C. Barth Netterfield,[7,8,9] Susan Redmond,[1] Jason D. Rhodes,[10] Jürgen Schmoll,[2] Mohamed M. Shaaban,[8,9] Ellen Sirks,[11] and Sut-Ieng Tam[3]

AFFILIATIONS

[1] Department of Physics, Princeton University, Jadwin Hall, Princeton, New Jersey 08544, USA
[2] Centre for Advanced Instrumentation (CfAI), Durham University, South Road, Durham DH1 3LE, United Kingdom
[3] Centre for Extragalactic Astronomy, Department of Physics, Durham University, Durham DH1 3LE, United Kingdom
[4] University of Toronto Institute for Aerospace Studies (UTIAS), 4925 Dufferin Street, Toronto, Ontario M3H 5T6, Canada
[5] Department of Astronomy/Steward Observatory, University of Arizona, 933 North Cherry Avenue, Tucson, Arizona 85721, USA
[6] Institute of Theoretical Astrophysics, University of Oslo, Blindern, Oslo 0315, Norway
[7] Department of Astronomy, University of Toronto, 50 St. George Street, Toronto, Ontario M5S 3H4, Canada
[8] Dunlap Institute for Astronomy and Astrophysics, University of Toronto, 50 St. George Street, Toronto, Ontario M5S 3H4, Canada
[9] Department of Physics, University of Toronto, 60 St. George Street, Toronto, Ontario M5R 2M8, Canada
[10] Jet Propulsion Laboratory (JPL), California Institute of Technology, 4800 Oak Grove Drive, Pasadena, California 91109, USA
[11] Institute for Computational Cosmology, Durham University, South Road, Durham DH1 3LE, United Kingdom
[12] Department of Physics and Astronomy, The University of Sheffield, Hounsfield Road, Sheffield S3 7RH, United Kingdom

[a] Author to whom correspondence should be addressed: javierr@princeton.edu

ABSTRACT

At a fraction of the total cost of an equivalent orbital mission, scientific balloon-borne platforms, operating above 99.7% of the Earth's atmosphere, offer attractive, competitive, and effective observational capabilities—namely, space-like seeing, transmission, and backgrounds—which are well suited for modern astronomy and cosmology. The Super-pressure Balloon-borne Imaging Telescope (SUPERBIT) is a diffraction-limited, wide-field, 0.5 m telescope capable of exploiting these observing conditions in order to provide exquisite imaging throughout the near-infrared to near-ultraviolet. It utilizes a robust active stabilization system that has consistently demonstrated a 48 mas 1σ sky-fixed pointing stability over multiple 1 h observations at float. This is achieved by actively tracking compound pendulations via a three-axis gimballed platform, which provides sky-fixed telescope stability at < 500 mas and corrects for field rotation, while employing high-bandwidth tip/tilt optics to remove residual disturbances across the science imaging focal plane. SUPERBIT's performance during the 2019 commissioning flight benefited from a customized high-fidelity science-capable telescope designed with an exceptional thermo- and opto-mechanical

stability as well as a tightly constrained static and dynamic coupling between high-rate sensors and telescope optics. At the currently demonstrated level of flight performance, SUPERBIT capabilities now surpass the science requirements for a wide variety of experiments in cosmology, astrophysics, and stellar dynamics.

I. INTRODUCTION

This paper presents the sub-arcsecond pointing and 50 mas image stabilization capabilities of the Super-pressure Balloon-borne Imaging Telescope (SUPERBIT) for diffraction-limited, wide-field near-infrared (NIR) to near-ultraviolet (NUV) imaging from a stratospheric balloon. This first section introduces the science objectives that motivate these imaging capabilities, with a high-level description of the system architecture from the perspective of mechanical, optical, and control systems engineering. Section II presents SUPERBIT's best achieved performance to date, from the 2019 telescope commissioning flight; Sec. III analyzes the key technical improvements that enabled this performance, learned through earlier engineering test flights; and Sec. IV predicts how the as-built performance could influence an observing strategy during SUPERBIT's upcoming long duration flight. The detailed science forecasts, based on the as-built performance, are being prepared for an accompanying *forecasting paper*.

A. Scientific applications

The SUPERBIT experiment is a balloon-borne telescope designed to provide diffraction-limited imaging over a $25' \times 17'$ field-of-view (approximately 36 times larger than the *Hubble Space Telescope*'s Advanced Camera for Surveys) with an on-sky resolution of <0.3 in. The platform utilizes the super-pressure balloon capabilities provided by the National Aeronautics and Space Administration (NASA), which offers mid-latitude long duration balloon (LDB) flights from 30 to 50+ days. A telescope at 36 km altitude is above 99.7% of the Earth's atmosphere,[1] enabling (1) potentially diffraction-limited observations, with negligible atmospheric "seeing" (<10 mas) and (2) space-like backgrounds and transmission throughout the wavelength range from the near-ultraviolet (300 nm) to the near-infrared (1000 nm).

Within this wavelength range, the projected resolution and depth of SUPERBIT imaging is sufficient to measure the (weak) gravitationally lensed shapes of distant (redshift $z \approx 1$) galaxies behind foreground ($z \approx 0.3$) clusters of galaxies.[2] Furthermore, SUPERBIT's wide field-of-view allows an entire cluster to be imaged in a single pointing, including its connection to the surrounding large-scale structure. With imaging available in six selectable bands from 300 nm to 1000 nm, UV/blue photometry—which is effectively inaccessible from the ground-based instruments—is particularly valuable for photometric redshift calibration, where cluster member galaxies can be identified via their 4000 A break or the 3700 A Balmer break in cluster dwarf galaxies for which this is suppressed.[2–4]

For multiple observations of 100–150 clusters over a single super-pressure balloon flight, the high-quality cluster weak lensing masses estimated with the SUPERBIT would allow for the computation of fundamental cosmological parameters such as σ_8 and Ω_m at the level of experiments including Weighing the Giants and

SPT-SZ.[5,6] In combination with x-ray or Sunyaev-Zoldovich (SZ) measurements, the SUPERBIT weak lensing maps of actively merging clusters would also be valuable for dark matter studies or calibration of cluster–mass observable relations. In addition, SUPERBIT's diffraction-limited imaging can mitigate de-blending calibration of the ground-based cosmological surveys like the Large Synoptic Survey Telescope (LSST),[7] reducing that particular source of systematic uncertainty and leading to tighter constraints on cosmological parameters.[8]

Given the ability for balloon-borne platforms like SUPERBIT to readily access, quickly implement, and flight verify cutting-edge technologies, high impact science goals can be realized at a fraction the economic and development time cost typical of equivalent space-borne implementations, with expected survey efficiencies rivaling similar ground-based applications. In addition to cluster cosmology, some examples of prospective science goals enabled by the SUPERBIT include probes of dark matter sub-structure, strong gravitational lensing constraints on the Hubble constant, studies of galaxies' morphological evolution, UV-bright stars, and exo-planetary atmospheres.

B. SUPERBIT architecture

The following is a brief description of the SUPERBIT instrument flown on the September 2019 science telescope commissioning flight, the last of a series of engineering test flights in advance of a long duration science mission. Detailed descriptions of the mechanical,[9,10] thermal,[11,12] control systems,[13–15] and software[13] architectures for the 2019 and previous test flight configurations are available in the literature.

1. Pointing and instrument stabilization

From a purely engineering perspective, the SUPERBIT platform, shown in Fig. 1, is a three-axis telescope stabilizer that is designed to provide a sub-arcsecond stability for the science payload, namely the 0.5 m NIR-to-NUV telescope, the scientific charge-coupled device (CCD) readout electronics, and accompanying back-end stabilization optics. A series of three gimballed frames provide sub-arcsecond stabilization and control, which together correct for both gravity-driven compound pendulations induced by the balloon and flight train as well as the bulk sky rotation for long exposures (300–600 s) over the science payload field-of-view (~0.5°). The gimbal roll and pitch control are facilitated per axis by frameless motors, each axially supported by flexure bearings that provide motion free from static friction, while a high-inertia reaction wheel facilitates the yaw control and pendulation stability, with excess momentum dumped through the flight train to the balloon via the pivot connection.[13]

Mounted to the science payload inner frame are two wide-angle (2–3°) star tracking cameras—one along the telescope boresight axis
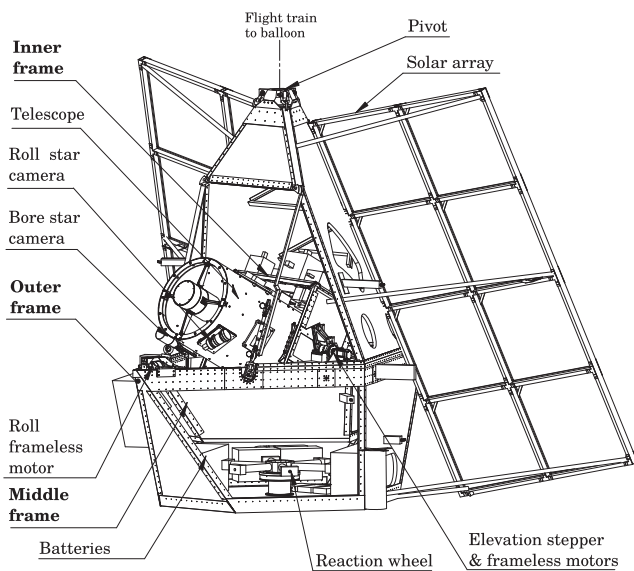
FIG. 1. The SUPERBIT 2019 gondola schematic representation with the primary stabilization components identified; total mass at the pivot is 800 kg, which includes CNES flight electronics; the SUPERBIT 2019 gondola has 1600 W solar power generation and 432 Ah power storage systems.

and the other orthogonal to it (i.e., the "roll" or "cross-boresight" star camera)—which provide absolute sky-fixed pointing references at up to 50 Hz, while 1 kHz rate gyroscopes (*KVH Industries, Inc.*) provide an inertial stabilization feedback. Altogether, science targets acquired with sub-arcminute-level accuracy are available with a full three-axis sub-arcsecond stability for 30–60 min per target, only limited mechanically by the roll and pitch gimbal throw ($\pm 6°$) and the full telescope pitch range ($20°$–$60°$).

In general, this level of sky-fixed, three-axis stability is distinct from other balloon-borne stabilizers that provide only a two-axis inertial stability[16] as well as balloon-borne scanners that only

require an accurate post-flight pointing reconstruction.[17,18] While the former (e.g., WASP[16]) is not suitable for wide-field imaging due to a field rotation (FR) drift, the latter only requires an in-flight pointing control at the $1'$ level necessary for obtaining star camera solutions on scan turnarounds, as is the case for the BLAST[17] and Spider[18] instruments. The SUPERBIT also differs from other highly stabilized suborbital instruments such as FIREBALL[19] in that the dominant external balloon-borne disturbance—an outer frame compound pendulation—is not actively damped but rather tracked by the gimbal system. As such, the SUPERBIT approach naturally allows for a reduction in the overall control effort—and therefore power—required to stabilize the science payload, while providing a tighter collocation in sensor-control feedback for instruments sensitive to structural resonances.[9,13]

2. Telescope optics and image stabilization

The SUPERBIT science telescope (Fig. 2) is a modified-Dall-Kirkham $f/11$ design with optics sensitive from 300 nm to 1000 nm (for a description of the pre-2019 engineering telescope, see 2015–2016 instrument papers[9,14]). As a highly custom-designed telescope (*Officina Stellare*), the 0.5 m conical primary (Zerodur), carbon-fiber monocoque body, and Invar components—namely, the secondary and lens stack mounting assemblies—mitigate potential thermal gradients across optical components of the telescope assembly as well as variable mechanical loading due to elevation maneuvers.

In addition, the three equilaterally placed linear actuators allow for the secondary mirror tip, tilt, and focus to be adjusted during operations to correct for the changes in alignment and primary focus after launch or from variations in the bulk temperature profile of the telescope assembly due to diurnal cycles. To correct for aberrations due to a spherical secondary mirror, a lens set near the back-end of the telescope assembly provides diffraction-limited imaging over a 55 mm focal plane with a 37.5 in./mm plate scale (~$0.5°$ usable field-of-view). Optics are thermally regulated through the telescope baffle to maintain a constant temperature profile and to mitigate large gradients when transitioning from day to night operations in the stratosphere.
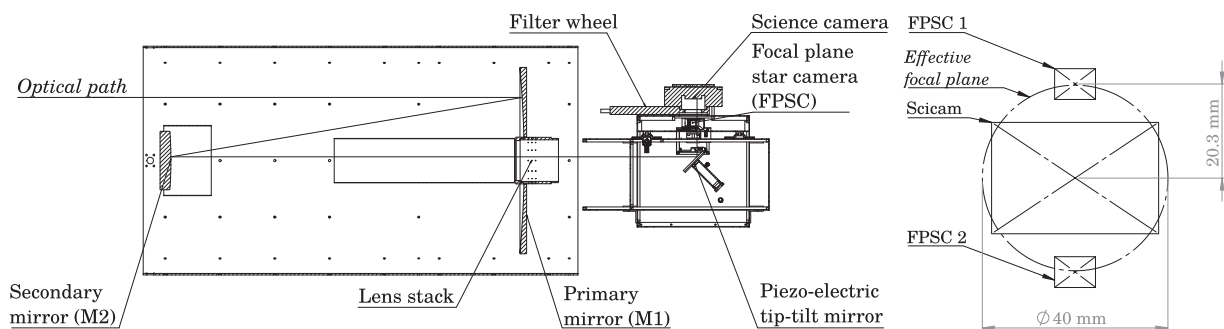
FIG. 2. (Left) A cross-sectional view of the SUPERBIT science telescope commissioned during the 2019 campaign; the primary structure comprised a solid carbon fiber monocoque configuration with Invar components to accommodate thermally sensitive elements (e.g., secondary mount); the telescope is mounted in the SUPERBIT inner frame on either side via opposing dovetail plates with a compliance in the radial, axial, and cross-pitch directions to mitigate differential thermal contractions between the telescope and the aluminum frame. (Right) The telescope focal plane layout including focal plane star cameras (FPSCs) and the science focal plane (scicam) with respect to the 40 mm diameter *effective* science-quality focal plane; the *usable* or *trackable* focal plane has a diameter of 55 mm, which includes a region of reduced beam quality only sufficient for tracking.

In order to provide further image stabilization at the science CCD, a piezo-electric tip-tilt actuated fold mirror provides high-bandwidth (50–60 Hz) focal plane corrections, which attenuate residual pointing jitter from the telescope stabilization systems down to 50 mas (1σ), well within the <0.3 in. optical diffraction limit (more details in Sec. III). A sky-fixed feedback for the tip-tilt actuator is provided by a pair of focal plane tracking star cameras (FPSCs)—one on either side of the science CCD—while low noise rate gyroscopes (*Emcore Corporation*) at 350 Hz mounted directly to the telescope structure provide inertial feedback while actively correcting for the bulk latency and the limited bandwidth of the FPSCs.

Overall, SUPERBIT's customized telescope design in conjunction with the three-axis tracking and stabilization platform is what enables a wide-field, diffraction-limited imaging in the near-IR to near-UV, a capability that had not yet been demonstrated from scientific balloon-borne payloads. The remainder of this paper discusses how the SUPERBIT has met this specification.

II. INSTRUMENT PERFORMANCE

The 2019 SUPERBIT science telescope commissioning flight began on September 17, 2019, at 20:34 GMT-4 with a launch support provided by the *Center National d'Études Spatiales* (CNES) through the Canadian Space Agency (CSA) from Timmins, Ontario (Fig. 3). After a 2 h ascent to a minimum float altitude of 27 km (89 kft), the SUPERBIT instrument was calibrated and aligned during the first 4 h of operations, which was followed by 3.5 h of science observations. Flight termination occurred on September 18, 2019, at approximately 14:00 GMT-4 after 7 h of daytime operations.

This section reports the best pointing and image stabilization performance achieved till date from the SUPERBIT 2019 flight, which includes the current SUPERBIT performance results for telescope pointing stabilization, target acquisition accuracy, and focal plane image stabilization throughout typical operations. To highlight particular challenges involved with demonstrating the achieved

FIG. 3. SUPERBIT pre-launch 2019 (site: Timmins, Ontario); during inflation of the primary balloon (bottom left), SUPERBIT is secured by the launch support vehicle (top) beneath the smaller tow balloon (bottom right); on launch, the tow balloon provides neutral buoyancy for the payload as the primary balloon is released and ascends above it.

level of performance, comparisons with pre-2019 engineering test flights are provided (additional details on pre-2019 performance are available in the literature[14,15]).

A. Telescope stabilization

As described in Subsection I B, the SUPERBIT telescope itself is stabilized about all three rotational degrees-of-freedom via a series of gimballed frames with inertial feedback from the rate gyroscopes and sky-fixed reference feedback from star tracking cameras. When a target is requested in right ascension (RA) and declination (Dec), the gimbals slew in unison to the calculated target gimbal angles in order to point the telescope to the corresponding azimuth (Az) and elevation (El) coordinates on the sky while offsetting the middle and inner frames (see Subsection II C) to maximize the tracking time on the sky with fixed field rotation (FR). Targets are typically acquired within 5 min of the request. Once a lost-in-space solution is acquired at the target coordinates,[20] the gimballed frames are iteratively honed toward the desired target until the absolute error on the sky is within a commandable star camera subframe threshold, which for SUPERBIT is typically $0.5'$. Following this, the star camera centroids are then used for a higher rate feedback, which provides absolute, sky-fixed stability while concurrently correcting for biases in the rate gyroscopes that provide inertial stability.

During the 2019 flight, the SUPERBIT tracked and stabilized over several telescope tracking runs for a number of alignment calibration and potential science targets of interest. For a typical long timescale telescope stabilization run (~0.5 h), Fig. 4 shows the centroid distribution plots in the boresight and cross-boresight star cameras as well as a representative point-spread-function (PSF) per tracking camera. Analyses and discussions on this level of sub-arcsecond pointing performance are provided in Subsection III A.

B. Image stabilization

Once telescope stabilization is established, a high-bandwidth, piezo-electrically actuated, tip-tilt fold mirror further stabilizes the focal plane. As described in Subsection I B, the sky-fixed feedback is obtained from a pair of focal-plane tracking star cameras, each equally separated about the center of the science camera CCD by 29.3 arc min (see Fig. 2). In addition to providing the inertial feedback, a set of low noise rate gyroscopes directly and rigidly coupled to the telescope frame itself increases the effective bandwidth and corrects the bulk image processing latencies inherent to each of the focal plane star cameras. Altogether, this tracking system comprises the fine guidance system (FGS).

To be able to effectively track the residual perturbations on the focal plane, the expected peak-to-peak variation from the telescope stabilization stage must be well within the maximum throw of the tip-tilt stage. With the knowledge of the 2019 back-end optics geometry, notably the distance between the tip-tilt stage and focal plane ($\ell = 169$ mm) and the maximum stage-centered throw of the FGS ($\theta = 2$ mrad), the maximum sky-equivalent pitch throw ϕ_{pitch} and cross-pitch throw ϕ_{xpitch} of the FGS are given by

$$\phi_{\text{pitch}} = p \cdot \ell \cdot \theta, \quad \phi_{\text{xpitch}} = \phi_{\text{pitch}} \cdot \cos(45 \deg), \quad (1)$$

$$\Rightarrow p = \frac{206264.8''}{D \times f}, \quad (2)$$
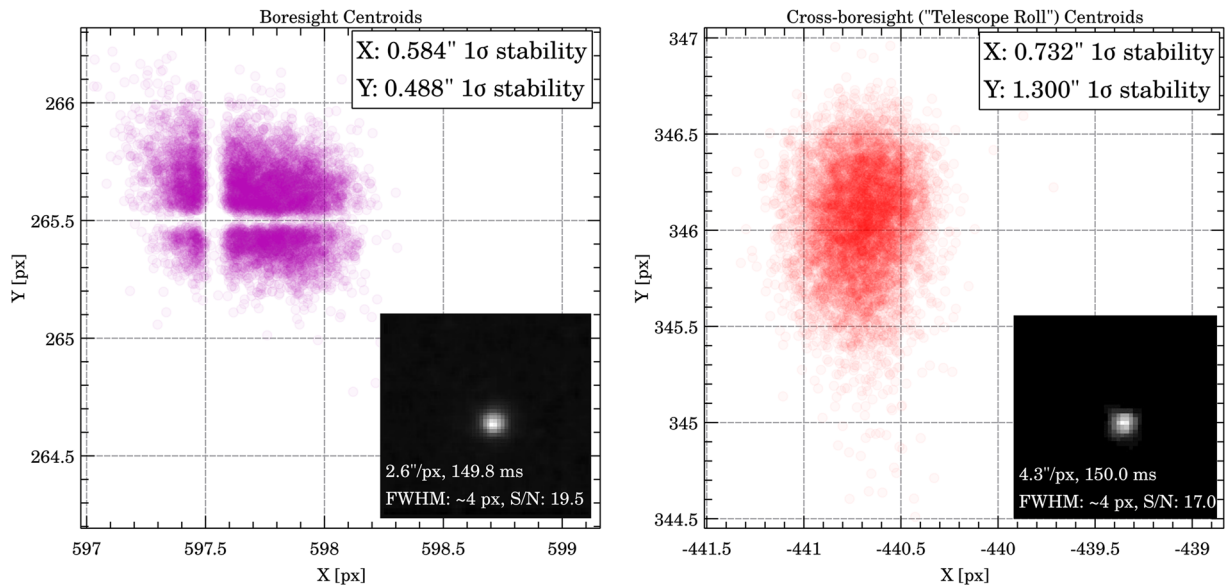
FIG. 4. Telescope pointing stability as measured by the boresight (left) and cross-boresight (right) star cameras during a typical long timescale telescope tracking run (>30 min) from the SUPERBIT 2019 flight, where each data point is a single sky-fixed star centroid; 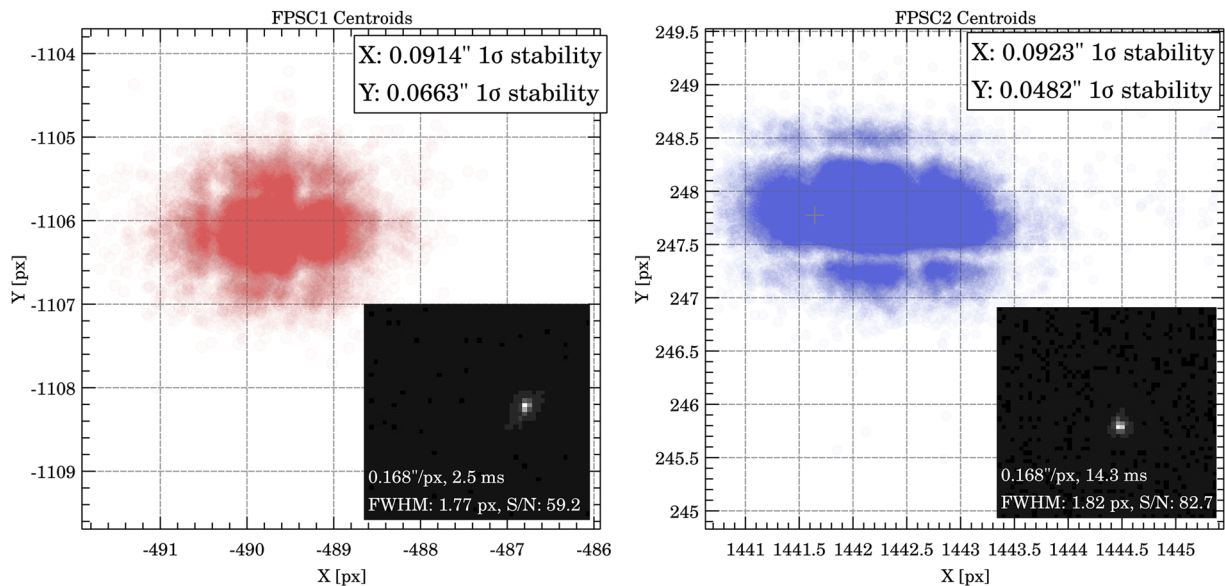typical star camera centroid thumbnails are shown, where boresight and cross-boresight sky-equivalent pixel scales are 2.6 in. and 4.3 in., respectively; sub-pixel structures (i.e., gaps between pixels) are clearly resolved at pixel boundaries (with a 0.5 px offset) due to a non-linear pixel response; 1σ pointing stability metrics are reported per camera (and per focal plane axis).

where $p = 0.168$ in./px is the FPSC plate scale, $D = 500$ mm is the primary mirror diameter, and $f = 11$ is the f-number for the SUPERBIT 2019 science telescope. Due to the 90° fold in the optical path (see Fig. 2), the effective throw of the cross-pitch axis is reduced by a factor $\cos(45°)$ compared to the pitch axis. To highlight the performance shown previously, the $\phi_{\text{pitch}} = 12.61$ in. and $\phi_{\text{xpitch}} = 8.92$ in. requirements on stabilization are at least 15 times the demonstrated 1σ telescope stabilization. Note, however, that this specification does

FIG. 5. Actively stabilized FGS tracking stability as measured by each of the focal plane star tracking cameras (FPSCs), where each data point is a single sky-fixed star centroid; one representative 6 min tracking run on FPSC1 (left) and FGS tracking on FPSC2 (right) during the telescope stabilization run in Fig. 4 are shown; typical star camera centroid thumbnails are shown, where the sky-equivalent pixel scale for each FPSC is 0.168 in.; sub-pixel structures (i.e., gaps between pixels) are clearly resolved at pixel boundaries (with a 0.5 px offset) due to a non-linear pixel response; 1σ pointing stability metrics are reported per camera (and per focal plane axis).

not include potentially long timescale mechanical or thermal drifts between the boresight and focal plane star cameras, since such variations are unknown at the telescope tracking level without feedback information from the tip-tilt stage. These longer timescale effects are reported in Subsection II C and further discussed in Sec. III.

Once trackable stars were reliably obtained on one or both of the FPSCs during the first half of the 2019 flight, the dedicated image stabilization runs calibrate the FGS and align the telescope optics. Figure 5 demonstrates the typical image stabilization performance post-calibration by evaluating a focal plane star camera centroid distributions as a sky-fixed metric for FGS corrections, in response to residual disturbances from the telescope stabilization stage. Discussions on FGS performance, including FPSC tracking depth, FPSC beam size, and overall image stability, are provided in Subsections III A and III B.
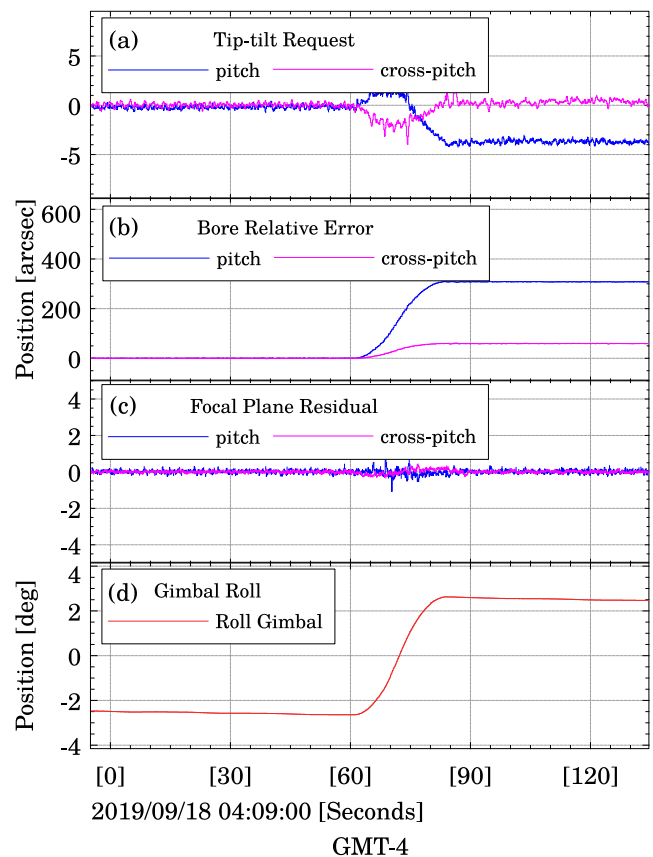
C. Target acquisition

To find adequate guide stars for image stabilization, the SUPERBIT stabilization platform must have a sufficiently accurate absolute pointing to place a target within the roughly $5.5' \times 4'$

field-of-view of either focal plane star camera. Although the pointing and tracking systems are capable of acquiring targets to a much higher precision (within the 0.26 in. star camera centroiding resolution), the SUPERBIT target acquisition requires only arcminute-level repeatability, because of its wide field-of-view and absolute sky-fixed feedback. If higher accuracy is required postflight, absolute pointing information can be reconstructed from flight data and confirmed directly with astrometry[20] on science camera images. Over the extended tracking runs, a relative drift between the boresight and focal plane star tracking cameras is shown in Fig. 6 to be minimal (< 10% the FGS throw), which contrasts the large 10–20 arc sec pointing drift observed during the pre-2019 test flights. This reflects both the thermo-mechanical and the opto-mechanical stability of the 2019 telescope optics, back-end optics, and star camera mounts, a detailed discussion of which is provided in Subsection III C. To quantify this effect, the sky-equivalent FGS command shown in Fig. 6 measures how the focal plane would have moved with respect to the boresight star
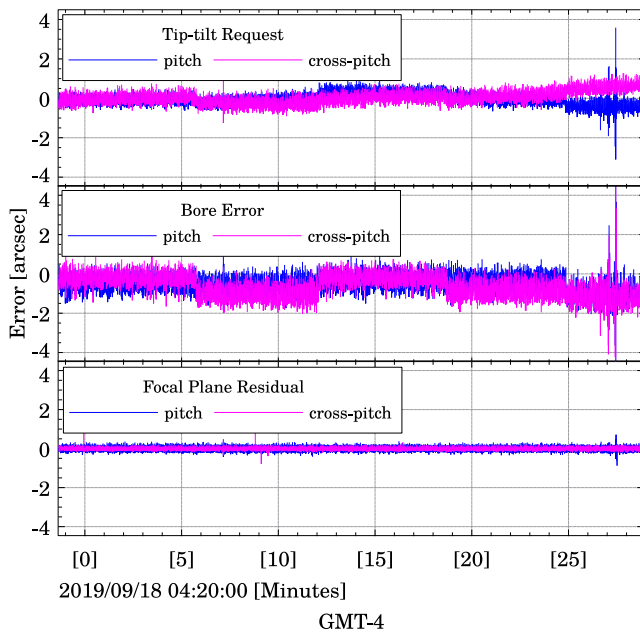
FIG. 6. (Top) An absolute pointing residual plot illustrating the drift of the FGS tip-tilt mirror command during the image stabilization run shown in Fig. 5; this is not the result of a telescope pointing drift, as would be seen by the bore star camera centroid residuals (middle), or a telescope focal plane drift, as would be seen by the FPSC centroid residuals (bottom), which implies that this is likely a relative pointing drift between the boresight star camera and the telescope focal plane; despite this, the <1 in. drift is maintained well within the 8.92 in. (or ±4.46 in.) cross-pitch throw of the FGS; on-sky directions for all residual plots are given in pitch and cross-pitch to distinguish from telescope El and cross-El; randomized commanded dithering steps can be seen at 5 min intervals (top and middle) but are removed by the FGS at the telescope focal plane (bottom).

FIG. 7. A target re-acquisition and continuous target tracking during simultaneous roll and fine pitch gimbal resets; gimbal frames track in unison about the FPSC target star while the FGS attenuates perturbations at the 2–4 in. level (a) down to <0.2 in. (c) during the reset; the boresight star camera centroids (b) show a mean shift post-reset due to an offset pointing vector with the FPSC(s) as the roll gimbal is slewing (d); the maximum sky-equivalent throw of the FGS in pitch and cross-pitch is 12.61 in. and 8.92 in., respectively.

camera had the FGS not been continuously correcting for structural or kinematic disturbances. Plausible sources for residual discrepancies between the optics and telescope pointing are discussed in Subsection III C.

For the SUPERBIT, target acquisition repeatability and target re-acquisition are also important factors contributing to an overall survey efficiency during science operations. In particular, a fixed-time overhead is required to reset the roll and pitch gimbals once either axis has reached its maximum usable throw, which is fundamentally limited by the flexure bearings (±6° smooth tracking range), as mentioned in Subsection I B. To minimize the time required to recover image stabilization after a reset, all three gimballed axes are slewed in unison about the FPSC target star in a way that resets the roll and pitch gimbals while maintaining the target star within the FGS full throw. Figure 7 demonstrates the efficacy of this approach from a typical gimbal reset during the SUPERBIT 2019 flight. During this kind of reset, which takes place over about 20 s, science camera exposures are temporarily halted, and the net effect on subsequent science camera exposures post-reset is a 1°–6° field rotation about the current tracking FPSC depending on the target.

III. ANALYSIS AND DISCUSSION

A. Telescope and image stabilization

As presented in Sec. II, telescope stabilization performed exceptionally well, where the maximum throw of the FGS is 15 times the worst-case 1σ pitch/cross-pitch pointing stability over even the longest tracking timescales. Even though the telescope roll stability was only maintained at the arcsecond level, as shown in Fig. 4, the sensitivity of the telescope focal plane to roll perturbations is significantly lower than in pitch and cross-pitch, where a 1 in. roll motion over a 0.5° angular separation between the telescope and the boresight star camera is <10 mas in the worst case. Furthermore, the fidelity of both telescope and image stabilization performance (in Figs. 4 and 5, respectively) is highlighted by the clear sub-pixel structure observed in the centroid distributions, where the finite size of the pixel gaps on the respective imaging sensors is clearly resolved near the pixel boundaries (with a 0.5 px offset).

1. Stabilization trade-offs

The high performance of the SUPERBIT telescope stabilization platform suggests that there may have been potential trade-offs between telescope stabilization and image stabilization that could have further improved the overall attenuation and fidelity of the FGS in correcting for the residual telescope disturbances. Figure 8 shows the zero-speed inertial stabilization (i.e., rate gyroscopes only) immediately following the tuning phase of the flight (a detailed controls description is available here[13]).

Comparing pitch and cross-pitch control, it is clear that there is a noticeable level of over-control in the pitch axis, which is characterized by the wide-band feature in the pitch spectrum centered at ~7 Hz. This idea of pitch over-control is supported by the fact that the pitch spectrum at low (<1 Hz) frequencies has been pushed below the noise floor seen at higher frequencies. Although there is some over-control in the cross-pitch axis as well, the cross-pitch over-control is 42% lower than in the pitch axis, which suggests that the pitch control gains may have been slightly over-tuned. The
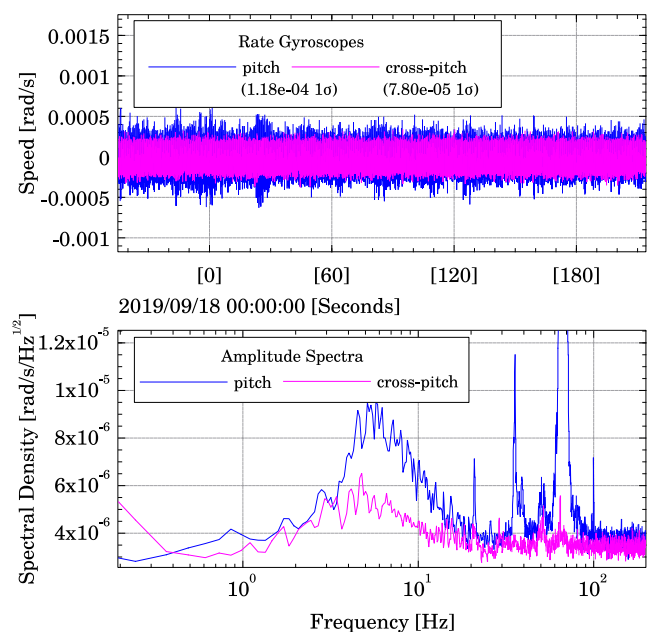
FIG. 8. Rate gyroscopes residuals after gain calibration of the telescope stabilization stage during the 2019 SUPERBIT telescope commissioning flight; timestreams (top) and amplitude spectra (bottom) are given in the telescope pitch and cross-pitch axes during a period where the gondola was only being inertially stabilized (i.e., rate gyroscopes controlled to zero speed with no sky-fixed feedback); the 1σ noise measured in the cross-pitch axis is 35% below the 1σ noise measure in pitch.

overall result of this over-tuning is a level of high frequency rate gyroscope noise from telescope stabilization leaking into the image stabilization stage.

In Fig. 5, this effect is directly observed in the 48% reduction in performance in the FGS pitch-oriented axis compared to the cross-pitch. It is therefore reasonable to assert that a reduction in pitch gains, although potentially reducing performance at the telescope stabilization stage at lower frequencies, would have reduced a higher frequency rate gyroscope noise that inadvertently degraded image stabilization in the pitch.

Overall, it is clear from the results that the 50 mas stability requirement was consistently achieved during flight in the cross-pitch, and despite the fact that there is indeed a clear asymmetry in FGS performance due to pitch over-control effects, the level to which the FGS performed is still sub-pixel on the science CCD and below the diffraction limit (< 0.3 in.). This level of performance met science requirements; partly due to time constraints, the 2019 performance was deemed adequate to begin science operations for the remainder of the 2019 flight. Additional tuning would have likely yielded an improved performance in the pitch axis and, potentially, in the image stabilization overall.

B. Diffraction-limited performance

1. FPSC beam size

The image stabilization results in Fig. 5 provide preliminary insights into the optical performance of the 2019 SUPERBIT science

telescope, which not only influences the quality of the resulting science images, but also is directly related to the limiting depth and fidelity of FGS centroiding and, therefore, focal plane tracking performance. To quantify the sharpness of the star imaged on the FPSCs, the full-width at half-maximum (FWHM—in pixels, denoted W) reported in flight (and shown in Fig. 5) is estimated by

$$\hat{W} = \frac{4 \log 2}{\pi} \sqrt{\frac{\sum_i p_i}{\max_i p_i}}, \qquad (3)$$

where $\sum_i p_i$ is the sum of all the pixels and $\max_i p_i$ is the maximum/peak pixel value in the background-subtracted image subframe. Typical FPSC exposure times are <200 ms.

Due to the small number of pixels that contribute to the sum post-background-subtraction, this estimator $\hat{W}$ is inherently subject to pixel noise and is potentially biased due to variation in background estimates. To correct for this bias, simulated Gaussian sources were tuned such that $\hat{W}$ and background noise matched those observed and measured during the flight. Over 10 000 simulations, the input FWHM (W) used to match the flight images were then used to generate a calibration curve given by $W \simeq 1.307\hat{W} - 0.705$. For the majority of the 2019 flight, the estimated FWHM values on FPSC2 were within the $\hat{W} = 1.7$–1.9 px range per image, which correspond to the bias-corrected FWHM values of $W = 1.52$–1.78 px or 0.255–0.300 in. on the sky. A representative measure of FWHM on FPSC1, which had considerably fewer image stabilization runs, is $\hat{W} = 1.75$ px corresponding to $W = 1.58$ px or 0.265 in. on the sky.

For a typical 300 s science camera exposure, Fig. 9 shows the co-added PSF on the FPSCs, which effectively captures the optical PSF convolved with the pixel response, and the measured pointing jitter during image stabilization. Fitting a two dimensional Gaussian to the PSF yields a cumulative 0.400 in. and 0.350 in. FWHM on FPSC1 and FPSC2, respectively. After deconvolving the pointing jitter with a FWHM from 0.113 to 0.217 in. based on Fig. 5, this implies an optical PSF with a 0.273–0.302 in. FWHM.

The expected FPSC PSF can be estimated from simulation by taking into account the effective throughput at the FPSC (Fig. 10) and integrating the nominal simulated optical beam per-band. From this, the theoretical pixel-convolved FWHM is 0.273 in. on the sky, which agrees with the measured value remarkably well compared to the best-case measured PSF on FPSC2 (<1%) and within 10% for the worst-case. Note that, given its broadband spectral response, the FPSC PSF is markedly wide compared to the typical PSF expected in many of the SUPERBIT science bands; however, the FPSCs provide a higher PSF spatial resolution due to 20% smaller pixels compared to the science camera.

As shown in Fig. 9, the measured PSF in the FPSCs on opposite sides of the field of view differ at a level of 50 mas, near the demonstrated limit of tracking stability. There are a variety of potential causes for this PSF variation. For example, a degree of optical misalignment may have been present at the secondary, causing an asymmetry in the aberrations at the location of the two FPSCs, which are offset 20.3 mm from the optical axis (Fig. 2). Pointing jitter over the FPSC exposure time is also convolved with the optical PSF per image, but the level to which this plays a role is limited by the short exposure times typical on the FPSCs (nominally <20 ms). Relative focus stages allow for FPSCs' focus positions to be calibrated independently, so the 15% broader PSF observed in FPSC1 compared to FPSC2 could be attributed to relative defocus between the two
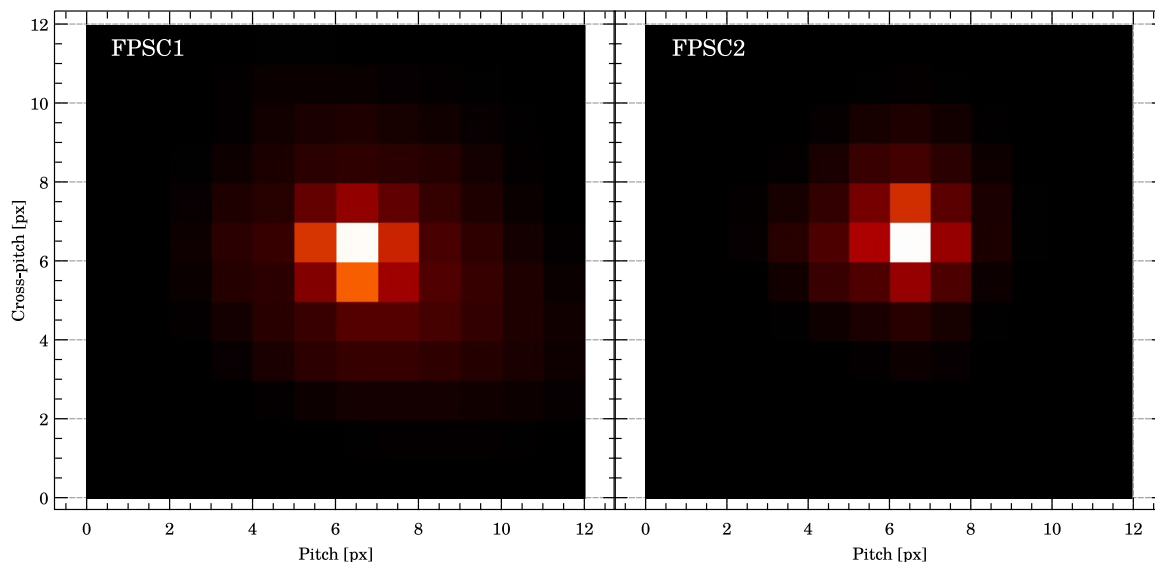
FIG. 9. Co-added FPSC PSFs integrated over typical science camera exposures during the image stabilization run from Fig. 5, which represents the combination of pointing jitter as well as the effective optical beam through the SUPERBIT science telescope optics; FPSC pixel scale is 0.168 in./px for a measured co-added FWHM of 0.400 in. on FPSC1 and 0.350 in. on FPSC2; correcting for pointing jitter at a FWHM of 0.113–0.217 in. yields an optical PSF FWHM of 0.273–0.302 in., which agrees well with the simulated diffraction-limited PSF.
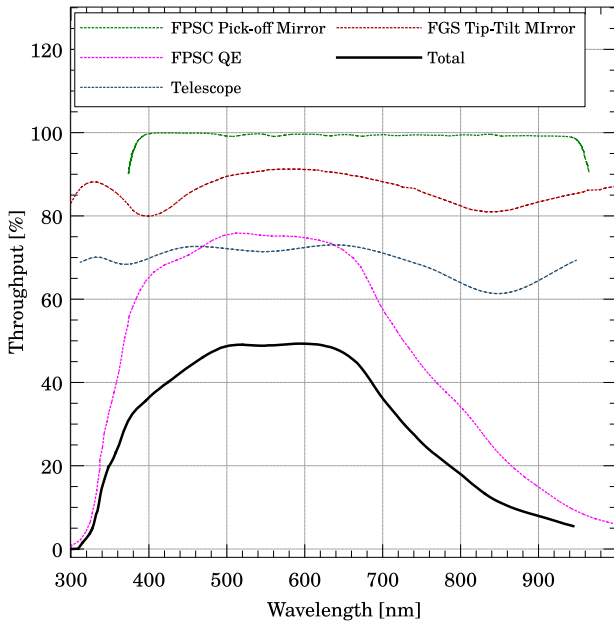
FIG. 10. Theoretical per-band optical efficiency at the FPSCs focal plane, which incorporates the following: optical characteristics, namely, the transfer curves for the primary mirror, secondary mirror, and the lens stack combined; back-end optical characteristics, including the tip-tilt fold mirror and the FPSC pick-off mirror; and the nominal FPSC quantum efficiency response. For a flat spectrum source, the effective band center of the FPSCs is 600 nm, with 89% bandwidth and a band-average throughput of 38%.

tracking camera sensors. All these can easily be improved through more regular calibration (e.g., daily) during a longer duration mid-latitude science flight.

2. FPSC tracking depth

Overall, an FPSC depth not only affects how well the FGS can effectively stabilize the telescope focal plane but also directly determines the availability of targets on the sky, where sensitivity to dimmer guide stars (i.e., higher apparent magnitude) increases the likelihood that a given target will have a trackable star on one or both of the FPSCs. As such, it is important to assess the limiting star magnitude that the SUPERBIT science telescope can use for image stabilization. This was not directly measured during the 2019 flight due to time constraints, but the limiting star magnitude can be estimated with the knowledge of system performance with the known guide stars on the FPSC. Specifically, Table I shows a summary of identified stars on the FPSCs at a given exposure time and signal-to-noise ratio (SNR) during unique image stabilization pointings during the 2019 flight. In terms of apparent magnitudes M, the gains from increased exposure time (t_{exp}) and decreased SNR (a_{snr}) can be estimated by

$$\Delta M_{exp,rn} = 2.5 \log\left(\frac{t_{exp,max}}{t_{exp}}\right), \qquad (4)$$

$$\Delta M_{exp,dc} = \frac{2.5}{2} \log\left(\frac{t_{exp,max}}{t_{exp}}\right), \qquad (5)$$

$$\Delta M_{snr} = 2.5 \log\left(\frac{a_{snr}}{a_{snr,min}}\right). \qquad (6)$$

TABLE I. Estimated tracking depth on the FPSCs based on uniquely identified guide stars from the SUPERBIT 2019 flight; the tracking depth or limiting magnitude is estimated based on the observed magnitude of the tracked star on the FPSC, which is then corrected based on magnitude gain ΔM_{snr} from the ability to track at reduced signal-to-noise; this is further corrected by estimated magnitude gain $\Delta M_{exp,rn}$ or $\Delta M_{exp,dc}$ from increased exposure times limited by read-noise or dark-current, respectively; a maximum exposure time $t_{exp,max} = 0.1$ s and minimum SNR $a_{snr,min} = 10$ is determined from simulation based on an effective 20 mas image stabilization resolution; observed magnitudes reference the GAIA DR2 catalog,[21] which has a similar band-pass to the overall effective throughput shown in Fig. 10.

Flight data			Magnitude estimation			
Observed mag.	t_{exp} (ms)	a_{snr}	$\Delta M_{exp,dc}$	$\Delta M_{exp,rn}$	ΔM_{snr}	Limiting mag.
8.7	14	79	1.0	2.1	2.2	12–13
8.9	19	70	0.9	1.8	2.1	12–13
8.7	11	85	1.2	2.4	2.3	12–14
6.0	1.0	80	2.5	5.0	2.3	11–13
6.6	3.0	54	1.9	3.8	1.8	10–12

Here, $\Delta M_{exp,rn}$ and $\Delta M_{exp,dc}$ bound the magnitude gain from an increased exposure time assuming either read-noise- or dark-current-limited exposures, respectively, where the latter yields reduced magnitude gain due to an increased noise that scales with $\sqrt{t_{exp}}$.

The minimum SNR is determined from the simulation based on the fidelity of the centroiding algorithm used on the FPSCs, which suggests that the required one-tenth pixel centroid accuracy (~20 mas) is adequately maintained with $a_{snr,min} = 10$. For a maximum exposure time, FGS simulations indicate that tracking stability—limited by rate gyroscope noise ($0.002°/\sqrt{hr}$)—is sufficiently constrained at the 20 mas level by FPSC centroid estimation at 10 Hz or $t_{exp,max} = 0.1$ s (see the control architecture[13]). Applying this to the 2019 tracking runs, Table I shows the limiting apparent magnitudes per target, with a flight average limiting magnitude range of 11–13. Surveying the GAIA DR2 star catalog[21] at a limiting magnitude ≤13, the FPSCs are within 1′ of a guide star over about 83% of the sky. When considering multiple angles of observation over the course of a night, this approaches 100% of the sky.

For more conservative estimates, future SUPERBIT science flights—such as a 30–50 day mid-latitude flight—would undoubtedly benefit from higher target availability over the full sky. As such, additional sensitivity could potentially be gained by improving the optical efficiency of the back-end optics or the FPSC CCD, where the former would be a trade-off for sensitivity in the shorter wavelength near-UV bands with alternative optical coatings. Improved target availability could also be achieved by increasing the proportion of the available telescope focal plane to FPSCs either through an increased area per FPSC or additional FPSCs distributed about the science CCD.

C. Telescope opto-mechanical and focus stability

1. Static pointing drift

The SUPERBIT engineering flights prior to the 2019 flight had observed that a relative pointing—specifically between the boresight

star camera and the main telescope—had drifted significantly over long (≥30 min) tracking periods. This effect had only been mitigated by the fact that the 10–15 in. net sky-equivalent drifts observed had only been 18.7% the full FGS throw in the pre-2019 configuration, where ϕ = 69.8 in. from (2) with f = 10, ℓ = 168 mm, and θ = 10 mrad.[14]

In contrast, the 2019 flight configuration performance results shown in Fig. 6 demonstrate much more stable relative pointing on the sky, with a worst case ≤1.0 in. sky-equivalent drift over the same time period or only 11.2% the full cross-pitch throw of the FGS. Note that compared to previous flight configurations, a 5 times reduction in the FGS range—as implemented for the 2019 flight—favors an improved position resolution over FGS throw. Although this implies that the 2019 FGS would not have been able to compensate for the larger relative drifts observed pre-2019, the more rigidly and optically coupled mounting of the boresight star camera directly to the carbon fiber telescope baffle tube played a major role in reducing drift over long timescales by an order of magnitude.

In addition to this effect, an apparent relative pointing drift can also be the product of relative motion between optical components within the telescope itself, namely, the primary and secondary mirrors shifting within their respective mounts due to thermal changes or changes in gravitational loading at different elevations. For the pre-2019 SUPERBIT test flights, the engineering telescope configuration utilized flexible, zero-stress mounting methods for optics (i.e., a whiffle tree with spring side supports) typically used for ground-based or certain space-based applications. However, the large deflections observed from the pre-2019 configurations may have also been indicative of a significant gravity sag and, consequently, gross optical misalignment. In contrast, the 2019 SUPERBIT science telescope, as described in Subsection I B, mitigates mechanical and thermal stresses through static mounting of a conical primary, which is, by design, rigid to within the structural flexibility of the solid carbon fiber monocoque shell at the $\lambda/20$ surface roughness requirement.

2. Relative dynamics

Although the static boresight camera mounting drift cannot be easily decoupled from the gravity sag of telescope and back-end optics, the relative dynamics between the telescope baffle (via rate gyroscopes) and FPSC centroids on the telescope focal plane can be directly compared. As such, Fig. 11 shows the spectra of the residual pitch and cross-pitch differences between the FPSC centroids and raw integrated rate gyroscopes, which are rigidly coupled to the telescope tube assembly. Since the measurement took place during periods when the FGS was disabled despite having a trackable star on the FPSCs, this measurement represents the difference in frequency response between the telescope frame and the optics, assuming that external effects (e.g., <0.010 in. stratospheric seeing) are negligible.

From the pre-2019 SUPERBIT test flights, a significant disagreement had been observed at the 0.2 in. level from 1 Hz to 15 Hz, where higher frequency motion had been captured by FPSC centroids, which was not reflected in the rate gyroscopes. To some level, this would imply that dynamic instability had been present between the telescope frame and telescope optics—likely due to the flexible primary mirror mount—which could have been driven by the telescope stabilization stage. In contrast, the 2019 flight results in Fig. 11 show a significantly improved agreement between the FPSC centroids and integrated rate gyroscopes and, therefore, suggest better optical and dynamic stability between the science telescope optics and baffle frame. Keeping in mind that $1/f$ drift is present in the raw integrated rate gyroscope timestreams, the sub-pixel agreement in amplitude spectra between the integrated rate gyroscopes and FPSC centroids is further emphasized by the similar shape and magnitude of variations in the timestreams from 0.5 Hz to 10 Hz. There does appear to be a slight residual below 0.5 Hz, but this can likely be attributed to spike removal in the timestreams (Emcore).
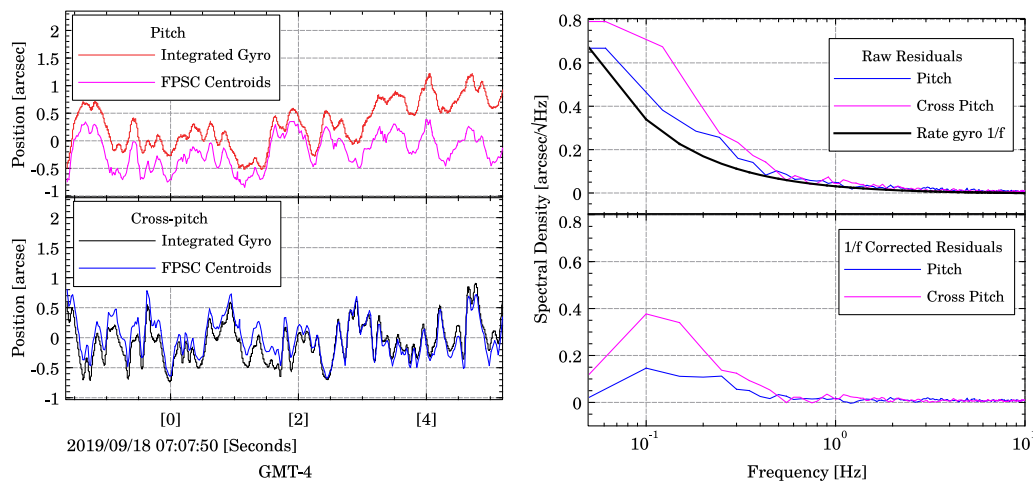
FIG. 11. Amplitude spectra of the computed difference between the SUPERBIT integrated rate gyroscopes and focal plane star camera centroids while the FGS tip-tilt stage is idle/not tracking (top right); gain differences and timing offsets between raw centroids and integrated rate gyroscopes are tuned manually with example timestreams compared in pitch (top left) and cross-pitch (bottom left); the $1/f$ component from raw rate gyroscope integration (top right, solid black curve) is estimated and subtracted off (bottom right) with comparisons made up to the nominal control bandwidth of the telescope stabilization stage (10 Hz); this shows a relatively good agreement between the integrated rate gyroscopes and focal plane centroids from 0.5 to 10 Hz.

When considering the static drift (Fig. 6), the relative dynamic stability (Fig. 11), and the overall image stabilization performance (Fig. 5), it is reasonable to assert—in contrast with the pre-2019 engineering test flights—that the SUPERBIT science telescope met mechanical stability specifications required to provide an effective sub-pixel image stabilization at a level sufficient for diffraction-limited imaging. Improvements in the rigidity of components' relative mounting or the fidelity of inertial measurements could potentially be informed by the direct measurement of the telescope optics motion during tracking (e.g., accelerometer measurements).

3. FGS depth-of-focus effects

For SUPERBIT's minimum wavelength in the near-UV (λ = 300 nm), the minimum delta focus ΔF to induce a quarter-wavelength wavefront error is given by

$$\Delta F \simeq \pm 2\lambda f^2, \tag{7}$$

where f is the f-number for the telescope. For the pre-2019 engineering telescope with a 55 mm diameter usable focal plane and $f = 10$, the $\theta = 10$ mrad full FGS throw could have potentially caused a defocus of 0.275 mm at the edge, which exceeds the $\Delta F = 0.060$ mm by nearly a factor of 5 had the full range been exercised. However, the maximum drift experienced from the previous test flights was only 18.7% of the full FGS throw equivalent to a maximum defocus of 0.514 mm, which had been within the tolerable ΔF albeit marginally.

In contrast, the 2019 science telescope and back-end optics configuration has a fivefold reduction in the FGS throw ($\theta = 2$ mrad) with a maximum defocus of 0.055 mm at the focal plane edge, which is comfortably within the $\Delta F = 0.0726$ mm tolerable delta focus for $f = 11$. For depth-of-focus, this implies significant margin for the maximum observed 1 in. absolute drift observed during the 2019 flight (Fig. 6), with nearly an order of magnitude more FGS throw than required to compensate.

For the 2019 science configuration overall, this ability to exercise the full FGS range highlights the flexibility in target re-acquisition accuracy during, for example, gimbal resets as shown in Fig. 7. Furthermore, this potentially enables the trading-off of telescope stabilization gains for an improved image stabilization, which may require the FGS to compensate for lower frequencies at high amplitude, as described previously. Should additional range during image stabilization be required, as was likely the case for the pre-2019 SUPERBIT configuration and could be the case for future

SUPERBIT flights for image dithering operations, FPSC centroid information could potentially be fed back to the telescope stabilization loop to mitigate larger low frequency perturbations. However, care would have be to taken to ensure sufficient decoupling with image stabilization (i.e., prevent co-servoed jack-knifing).

IV. SUMMARY AND FORECASTING

Table II shows the progression of SUPERBIT performance over 4 test flights from 2015 to 2019 compared to the most recent science telescope commissioning flight in September 2019. As previously mentioned, a major factor contributing to the improved performance of the SUPERBIT 2019 flight compared with previous test flights was the design, implementation, and flight verification of the SUPERBIT diffraction-limited telescope (Fig. 2), which provided the necessary opto-mechanical static and dynamic stability as well as optical beam quality (Fig. 9) required for a sufficiently robust focal plane stability. This is clearly reflected in the image stabilization results for 2019 (Fig. 5), where the performance over 5 min timescales is maintained over entire telescope tracking runs (Fig. 4) at the 30–60 min timescale. Improvements in the 2019 opto-mechanical design and relative mounting stiffness allowed for a higher resolution in the image stabilization stage over a smaller range compared to the engineering test flights (Subsection III C).

From the latest 2019 performance, the level of image stability achieved has been shown to be sufficient for diffraction-limited imaging from over SUPERBIT's wavelength range (300–1000 nm) (Subsection III B). As discussed in Subsection III A, the 2019 flight performance could have been improved with more time allocated to trading-off the coarse stabilization loop performance at lower frequencies for a reduced high frequency rate gyroscope noise that perturbed image stabilization (Fig. 8) through a careful gain reduction. For the prospective SUPERBIT mid-latitude LDB flight, this is effectively mitigated by the availability of additional calibration time on the sky as well as more opportunity for iteration with feedback from science images, both of which were quite limited by less than 8 h of operational time at float in 2019.

Ultimately, the optical and mechanical performances of the SUPERBIT science telescope and gondola will determine the effective science yield, specifically the number of clusters observed in the case of weak lensing. The achievable depth on the science camera

TABLE II. Summary of the best achieved 3-axis absolute pointing and image stabilization performance for the 4 SUPERBIT test flights over 5 years; stability over timescales representative of science camera integration periods (5 min) are reported in addition to stability over extended periods (30 min).

| | | | Best achieved sky-fixed stability (1σ) (arc sec) | | | |
| | | | Telescope stabilization | | Image stabilization | |
Year	Launch site	Provider	@ 5 min	@ 30 min	@ 5 min	@ 30 min
2015	Timmins, ON	CNES-CSA	0.5	1.5	0.085	0.5
2016	Palestine, TX	CSBF-NASA	0.5	1.1	0.070	0.2
2017/18	Palestine, TX	CSBF-NASA	0.4	0.8	0.065	0.090
2019	Timmins, ON	CNES-CSA	0.3	0.5	0.046	0.048

focal plane based on the telescope throughput will directly influence overall survey efficiency source completeness, while the PSF contributions from pointing jitter, optical alignment, and non-linear focal plane effects will impact the fidelity of background galaxy ellipticities at the 1%–3% level (estimated). Although certain aspects of these science-related factors are explored in the work presented here, further work is currently being undertaken to fully assess the SUPERBIT weak lensing potential as well as other science forecasting. This ongoing and future work will be captured in an upcoming *SUPERBIT forecasting paper*, in which the results of this work will be directly leveraged.

REFERENCES

[1] U. S. Atmosphere, *National Aeronautics and Space Administration* (United States Air Force, Washington, DC, 1976).

[2] R. Massey, C. Heymans, J. Bergé, G. Bernstein, S. Bridle, D. Clowe, H. Dahle, R. Ellis, T. Erben, M. Hetterscheidt, F. W. High, C. Hirata, H. Hoekstra, P. Hudelot, M. Jarvis, D. Johnston, K. Kuijken, V. Margoniner, R. Mandelbaum, Y. Mellier, R. Nakajima, S. Paulin-Henriksson, M. Peeples, C. Roat, A. Refregier, J. Rhodes, T. Schrabback, M. Schirmer, U. Seljak, E. Semboloni, and L. van Waerbeke, Mon. Not. R. Astron. Soc. **376**, 13 (2007); arXiv:astro-ph/0608643.

[3] W. Jones, "SuperBIT: Wide-field, sub-arcsecond imaging from the super-pressure balloon platform," NASA APRA Proposal, 2014.

[4] F. B. Abdalla, A. Amara, P. Capak, E. S. Cypriano, O. Lahav, and J. Rhodes, Mon. Not. R. Astron. Soc. **387**, 969 (2008); arXiv:0705.1437 [astro-ph].

[5] S. Bocquet, A. Saro, J. J. Mohr, K. A. Aird, M. L. N. Ashby, M. Bautz, M. Bayliss, G. Bazin, B. A. Benson, L. E. Bleem, M. Brodwin, J. E. Carlstrom, C. L. Chang, I. Chiu, H. M. Cho, A. Clocchiatti, T. M. Crawford, A. T. Crites, S. Desai, T. de Haan, J. P. Dietrich, M. A. Dobbs, R. J. Foley, W. R. Forman, D. Gangkofner, E. M. George, M. D. Gladders, A. H. Gonzalez, N. W. Halverson, C. Hennig, J. Hlavacek-Larrondo, G. P. Holder, W. L. Holzapfel, J. D. Hrubes, C. Jones, R. Keisler, L. Knox, A. T. Lee, E. M. Leitch, J. Liu, M. Lueker, D. Luong-Van, D. P. Marrone, M. McDonald, J. J. McMahon, S. S. Meyer, L. Mocanu, S. S. Murray, S. Padin, C. Pryke, C. L. Reichardt, A. Rest, J. Ruel, J. E. Ruhl, B. R. Saliwanchik, J. T. Sayre, K. K. Schaffer, E. Shirokoff, H. G. Spieler, B. Stalder, S. A. Stanford, Z. Staniszewski, A. A. Stark, K. Story, C. W. Stubbs, K. Vanderlinde, J. D. Vieira, A. Vikhlinin, R. Williamson, O. Zahn, and A. Zenteno, Astrophys. J. **799**, 214 (2015).

[6] A. B. Mantz, A. von der Linden, S. W. Allen, D. E. Applegate, P. L. Kelly, R. G. Morris, D. A. Rapetti, R. W. Schmidt, S. Adhikari, M. T. Allen, P. R. Burchat, D. L. Burke, M. Cataneo, D. Donovan, H. Ebeling, S. Shandera, and A. Wright, Mon. Not. R. Astron. Soc. **446**, 2205 (2015); arXiv:1407.4516 [astro-ph.CO].

[7] J. Rhodes, R. C. Nichol, É. Aubourg, R. Bean, D. Boutigny, M. N. Bremer, P. Capak, V. Cardone, B. Carry, C. J. Conselice, A. J. Connolly, J.-C. Cuilland re, N. A. Hatch, G. Helou, S. Hemmati, H. Hildebrandt, R. Hložek, L. Jones, S. Kahn, A. Kiessling, T. Kitching, R. Lupton, R. Mand elbaum, K. Markovic, P. Marshall, R. Massey, B. J. Maughan, P. Melchior, Y. Mellier, J. A. Newman, B. Robertson, M. Sauvage, T. Schrabback, G. P. Smith, M. A. Strauss, A. Taylor, and A. Von Der Linden, Astrophys. J. Suppl. Ser. **233**, 21 (2017).

[8] Planck Collaboration, N. Aghanim, Y. Akrami, M. Ashdown, J. Aumont, C. Baccigalupi, M. Ballardini, A. J. Banday, R. B. Barreiro, N. Bartolo, S. Basak, R. Battye, K. Benabed, J. P. Bernard, M. Bersanelli, P. Bielewicz, J. J. Bock, J. R. Bond, J. Borrill, F. R. Bouchet, F. Boulanger, M. Bucher, C. Burigana, R. C. Butler, E. Calabrese, J. F. Cardoso, J. Carron, A. Challinor, H. C. Chiang, J. Chluba, L. P. L. Colombo, C. Combet, D. Contreras, B. P. Crill, F. Cuttaia, P. de Bernardis, G. de Zotti, J. Delabrouille, J. M. Delouis, E. Di Valentino, J. M. Diego, O. Doré, M. Douspis, A. Ducout, X. Dupac, S. Dusini, G. Efstathiou, F. Elsner, T. A. Enßlin, H. K. Eriksen, Y. Fantaye, M. Farhang, J. Fergusson, R. Fernandez-Cobos, F. Finelli, F. Forastieri, M. Frailis, A. A. Fraisse, E. Franceschi, A. Frolov, S. Galeotta, S. Galli, K. Ganga, R. T. Génova-Santos, M. Gerbino, T. Ghosh, J. González-Nuevo, K. M. Górski, S. Gratton, A. Gruppuso, J. E. Gudmundsson, J. Hamann, W. Handley, F. K. Hansen, D. Herranz, S. R. Hildebrandt, E. Hivon, Z. Huang, A. H. Jaffe, W. C. Jones, A. Karakci, E. Keihänen, R. Keskitalo, K. Kiiveri, J. Kim, T. S. Kisner, L. Knox, N. Krachmalnicoff, M. Kunz, H. Kurki-Suonio, G. Lagache, J. M. Lamarre, A. Lasenby, M. Lattanzi, C. R. Lawrence, M. Le Jeune, P. Lemos, J. Lesgourgues, F. Levrier, A. Lewis, M. Liguori, P. B. Lilje, M. Lilley, V. Lindholm, M. López-Caniego, P. M. Lubin, Y. Z. Ma, J. F. Macías-Pérez, G. Maggio, D. Maino, N. Mandolesi, A. Mangilli, A. Marcos-Caballero, M. Maris, P. G. Martin, M. Martinelli, E. Martínez-González, S. Matarrese, N. Mauri, J. D. McEwen, P. R. Meinhold, A. Melchiorri, A. Mennella, M. Migliaccio, M. Millea, S. Mitra, M. A. Miville-Deschênes, D. Molinari, L. Montier, G. Morgante, A. Moss, P. Natoli, H. U. Nørgaard-Nielsen, L. Pagano, D. Paoletti, B. Partridge, G. Patanchon, H. V. Peiris, F. Perrotta, V. Pettorino, F. Piacentini, L. Polastri, G. Polenta, J. L. Puget, J. P. Rachen, M. Reinecke, M. Remazeilles, A. Renzi, G. Rocha, C. Rosset, G. Roudier, J. A. Rubiño-Martín, B. Ruiz-Granados, L. Salvati, M. Sandri, M. Savelainen, D. Scott, E. P. S. Shellard, C. Sirignano, G. Sirri, L. D. Spencer, R. Sunyaev, A. S. Suur-Uski, J. A. Tauber, D. Tavagnacco, M. Tenti, L. Toffolatti, M. Tomasi, T. Trombetti, L. Valenziano, J. Valiviita, B. Van Tent, L. Vibert, P. Vielva, F. Villa, N. Vittorio, B. D. Wand elt, I. K. Wehus, M. White, S. D. M. White, A. Zacchei, and A. Zonca, arXiv:1807.06209 (2018).

[9] L. Li, "The frequency and modal system identification of the balloon-borne imaging testbed," M.S. thesis, University of Toronto, 2016.

[10] L. Li, C. J. Damaren, L. J. Romualdez, C. B. Netterfield, J. W. Hartley, M. N. Galloway, R. J. Massey, and P. Clark, J. Aerosp. Eng. **29**, 04016051 (2016).

[11] S. Redmond, "Thermal design and control for stratospheric balloon-borne telescopes," M.S. thesis, University of Toronto, 2018.

[12] S. Redmond, S. Benton, A. M. Brown, P. Clark, C. J. Damaren, T. Eifler, A. A. Fraisse, M. N. Galloway, J. W. Hartley, M. Jauzac, W. C. Jones, L. Li, T. V. Luu, R. J. Massey, J. McCleary, C. B. Netterfield, J. D. Rhodes, L. J. Romualdez, J. Schmoll, and S.-I. Tam, Proc. SPIE **10700**, 1687–1696 (2018).

[13] L. J. Romualdez, "Design, implementation, and operational methodologies for sub-arcsecond attitude determination, control, and stabilization of the super-pressure balloon-borne imaging telescope (SuperBIT)," Ph.D. thesis, Institute for Aerospace Studies (UTIAS) and Department of Physics, University of Toronto, 2018.

[14] L. J. Romualdez, C. J. Damaren, L. Li, M. N. Galloway, J. W. Hartley, C. B. Netterfield, P. Clark, and R. J. Massey, IMech: J. Aerosp. Eng. **231**, 713 (2016).

[15] L. J. Romualdez, S. J. Benton, A. M. Brown, P. Clark, C. J. Damaren, T. Eifler, A. A. Fraisse, M. N. Galloway, J. W. Hartley, M. Jauzac, W. C. Jones, L. Li, T. V. T. Luu, R. J. Massey, J. Mccleary, C. B. Netterfield, S. Redmond, J. D. Rhodes, J. Schmoll, and S.-I. Tam, Proc. SPIE **10702**, 222–236 (2018).

[16] F. Kislat et al., J. Astron. Inst. **6**, 1740003 (2017); arXiv:1701.04536.

[17] E. Pascale, P. Ade, J. Bock, E. Chapin, J. Chung, M. Devlin, S. Dicker, M. Griffin, J. Gundersen, M. Halpern, P. Hargrave, D. Hughes, J. Klein, C. MacTavish, G. Marsden, P. Martin, T. Martin, P. Mauskopf, C. Netterfield, and D. V. Wiebe, Astrophys. J. **681**, 400 (2008).

[18] J. A. Shariff, P. A. R. Ade, M. Amiri, S. J. Benton, J. J. Bock, J. R. Bond, S. A. Bryan, H. C. Chiang, C. R. Contaldi, B. P. Crill, O. P. Doré, M. Farhang, J. P. Filippini, L. M. Fissel, A. A. Fraisse, A. E. Gambrel, N. N. Gandilo, S. R. Golwala, J. E. Gudmundsson, M. Halpern, M. Hasselfield, G. C. Hilton, W. A. Holmes, V. V. Hristov, K. D. Irwin, W. C. Jones, Z. D. Kermish, C. L. Kuo, C. J. MacTavish, P. V. Mason, K. G. Megerian, L. Moncelsi, T. A. Morford, J. M. Nagy, C. B. Netterfield, R. O'Brient, A. S. Rahlin, C. D. Reintsema, J. E. Ruhl, M. C. Runyan, J. D. Soler, A. Trangsrud, C. E. Tucker, R. S. Tucker, A. D. Turner, A. C. Weber, D. V. Wiebe, and E. Y. Young, Proc. SPIE **9145**, 297–316 (2014).

[19] J. Montel, F. Mirc, E. Pérot, I. Zenone, J.-M. Nicot, N. Bray, A. Gomes, J. Evrard, P. Tapie, P. Vola, B. Milliard, R. Grange, and D. Schiminovich, "Design and improvements of the attitude control system of the FIREBall balloon experiment," Proc. SPIE **9905**, 99053I (2016).

[20] D. Lang, D. W. Hogg, K. Mierle, M. Blanton, and S. Roweis, Astron. J. **139**, 1782–1800 (2010).

[21] A. Brown, A. Vallenari, T. Prusti, J. de Bruijne, C. Babusiaux, C. Bailer-Jones, M. Biermann, D. Evans, L. Eyer, F. Jansen, C. Jordi, S. Klioner, U. Lammers, L. Lindegren, X. Luri, F. Mignard, C. Panem, D. Pourbaix, and S. Randich, Astron. Astrophys. **616**, A9 (2018).

[22] W. A. Joye and E. Mandel, "New features of SAOImage DS9," in *Astronomical Data Analysis Software and Systems XII*, ASP Conference Series Vol. 295, edited by H. E. Payne, R. I. Jedrzejewski, and R. N. Hook (ASP, 2003), p. 489.

[23] E. Bertin and S. Arnouts, Astron. Astrophys. **117**, 393 (1996).